

Weak Line Water Vapor Spectra in the Region 13 200–15 000 cm⁻¹

Roland Schermaul,^{*} Richard C. M. Learner,^{*,1} A. A. D. Canas,[†] J. W. Brault,[†] Oleg L. Polyansky,^{‡,2}
Djedjiga Belmiloud,[‡] Nikolai F. Zobov,^{‡,2} and Jonathan Tennyson,^{‡,3}

^{*}Laser Optics & Spectroscopy, Blackett Laboratory, Imperial College of Science, Technology and Medicine, Prince Consort Road, London SW7 2BW, United Kingdom; [†]LASP (Space Technology Building), 1234 Innovation Drive, Boulder, Colorado 80303-7814; and [‡]Department of Physics and Astronomy, University College London, Gower Street, London WC1E 6BT, United Kingdom

E-mail: j.tennyson@ucl.ac.uk

Received May 18, 2001; in revised form September 24, 2001

New Fourier transform spectra of water vapor are presented in the range 6500–16 400 cm⁻¹ obtained using pathlengths of up to 800 m and long integration times. These spectra have a significantly higher signal-to-noise than previous measurements in this wavenumber range. Wavenumbers, absolute intensities and self-broadening coefficients all with associated uncertainties, are presented for 3604 lines in the region 13 200–15 000 cm⁻¹. Analysis of these lines using variational line lists, along with other unassigned lines from previous studies, has been conducted. This leads to 952 new line assignments to transitions involving 35 different vibrational states of H₂¹⁶O. A smaller number of lines are assigned to H₂¹⁸O and H₂¹⁷O. © 2002 Elsevier Science (USA)

Key Words: water vapor; near-infrared and visible spectrum; line assignments; line intensities; self-broadening coefficients

1. INTRODUCTION

There is at present a serious discrepancy between the observed and the modeled values of the atmospheric radiation budget (1, 2). The difference, in the simplest case—a clear sky—is of order 8%, and appears to be due to additional absorption in the visible and near infrared. Resolving this problem is important, not only in its own right but also because it is much larger than the probable change in the magnitude of greenhouse effects and thus has an impact on the credibility of this very serious topic. Among the possible causes is absorption due to a large number of (as yet unobserved) weak lines in the water vapor spectrum. A simple statistical analysis of the known part of the water spectrum suggests that unobserved weak lines in the red part of the spectrum (13 200–16 500 cm⁻¹) could contribute about 2.5 to 3% additional opacity (3); in the rest of the visible region the contribution should be of order 8 to 11%.

Using a long-path absorption cell and a visible/infrared Fourier transform spectrometer (FTS), we have made observations of the spectrum of water with a detection limit considerably better than that achieved in previous studies. We aimed to have both the cell and the FTS working at the limit of their performance. Very-high-reflectance optics for both the long-path cell and the auxiliary optics were employed in order to achieve optical path lengths of up to 800 m, which requires about 100 reflections. Modification to the FTS detector head amplifies

and electrical filter are described—these are essential to guarantee photon-noise-limited performance. In addition to these technical moves it was also necessary to use narrow band optical filter and long integration times. This strategy delivered spectra with a signal-to-noise ratio of order 3500:1 compared with a value of around 1250:1 realized in published work (4–12), allowing reliable line parameters, including line intensities, to be extracted for many weak water lines. This issue has taken on particular significance since concerns have been raised about water line intensities in the near infrared and visible (13–16) used in standard databases such as HITRAN (17). In this paper we present details of new experimental measurements and detailed analysis of the region 13 200–15 000 cm⁻¹, which covers the 4ν and 4ν + δ polyads of water. This analysis shows that the new spectra did indeed probe significantly deeper than previous studies.

2. EXPERIMENTAL DETAILS

2.1. Measurements

A series of water vapor absorption spectra were recorded from the near-infrared to the visible (6500–16 400 cm⁻¹ in total) using the combination of a high-resolution Fourier transform spectrometer (FTS, Bruker IFS 120HR) and a long-path absorption cell (LPAC) at the Rutherford Appleton Laboratory (RAL) Molecular Spectroscopy Facility.

The experimental goal was to attain the best possible signal quality; to this end great care was taken over the configuration alignment, and setup of the experiment, and certain parts of the hardware were modified as detailed below.

¹ Deceased.

² Permanent address: Institute of Applied Physics, Russian Academy of Science, Uljanov Street 46, Nizhnii Novgorod, Russia 603024.

³ Author to whom all correspondence should be addressed.

2.1.1. FTS Configuration

Before any recording could take place it was found necessary to realign the IFS 120 HR FTS from scratch; this corrected previous errors in the wavenumber scale and improved both throughput and resolution. The source was a 150-W tungsten halogen lamp run from a stabilized DC supply whose voltage was adjusted to slightly below the lamp's rating to improve lifetime and aging characteristics. This source gives maximal photon flux in the near infrared, and the spectrum falls away rapidly at higher wavenumbers. The FTS condenser and input aperture were adjusted carefully to ensure uniform bright illumination, the aperture diameter being selected to match the desired resolving power.

The FTS optical bandwidth was restricted by using combinations of interferometric "edge" filters (supplied by Corion). Each filter was fitted with a precision antireflection coated glass wedge to avoid potential channeling caused by stray reflections off the faces. Optical bandwidths were set to match the wavenumber range (or alias width) of each scan in order to avoid photon noise from adjacent wavelengths where (potentially) the source might be much stronger. This step is essential for low-noise operation and cannot be achieved using electrical filtration at the postdetector stage.

A dielectric-coated quartz beam splitter was used for measurements in the region $9500\text{--}16\,500\text{ cm}^{-1}$, while a coated CaF_2 beam splitter provided better performance in the region $6500\text{--}10\,500\text{ cm}^{-1}$. After careful alignment of the reference corner-reflector, fringe modulations were observed of approximately 75% in the region $9500\text{--}16\,500\text{ cm}^{-1}$ and 90% in the region $6500\text{--}10\,500\text{ cm}^{-1}$.

The FTS itself was evacuated using a turbomolecular pump to a pressure of 0.4 Pa to remove water vapor from the optical path.

2.1.2. LPAC Configuration

The LPAC (a White cell); described in detail previously (18), was configured with silver/dielectric coated high-reflectance mirrors and antireflection coated glass windows. Additionally, all mirrors in the input and output transfer optics used the same high-reflectance coatings, which exhibit better than 99% reflectivity in the region $700\text{--}1100\text{ nm}$ (supplied by Tayside Optical Technology, Dundee, U.K.). High reflectivity is crucial for overall throughput in a White cell when so many reflections (about 50) are involved.

Unfortunately the LPAC suffers from considerable mechanical instability, a lack of reference marks for alignment, and an inflexible transfer optics system. A collimated beam was brought to a focus as close as possible to one side of the large LPAC mirror; the quality of this focus was limited principally by the poor surface figure of the (diamond-turned) input collimator of the FTS. The two mirrors at the far end of the cell were then adjusted together to obtain successively greater path lengths, and the signal received at the output was plotted as a function of

the number of reflections. This allowed the effective reflectivity of the mirrors to be checked and also tracking of the effects of aberrations at higher path lengths. This check also proved useful later in detecting contamination. Although paths of up to 960 m were achieved with good throughput, they proved frustratingly impossible to take advantage of due to mechanical instability. Shorter paths around 800 m were selected as a compromise.

Light emerging from the LPAC was brought to a focus on the selected detector and considerable care was taken to check the alignment and stability of this focus.

Both input and output transfer optics were evacuated to a pressure of 0.02 Pa by a rotary/diffusion pump combination. The effects of pumping down on stability and throughput were checked and compensated.

2.1.3. Detection and Scanning

The standard Bruker detectors were discarded in favor of custom detector units designed utilizing high-quality photodiodes (Hamamatsu). Detector areas (typically $7\text{ to }8\text{ mm}^2$) were chosen to match the size of the beam focus after the LPAC, with an extra allowance for mechanical instability. An optimum detector was selected for each wave-band of interest (silicon in the visible and InGaAs in the near IR), with preference for PIN types where possible. Each detector was operated photo-ampereally (zero bias) by a low-current-noise operational amplifier (OPA129) and followed by a low-noise buffer amplifier to drive the cables. The transimpedance (or gain) was optimized before each run to give a near-full-scale signal to the digitizer, allowing for lamp brightening and other drifts throughout the run. The gain having been adjusted, feedback capacitances on the amplifier were adjusted to ensure optimum temporal response (with minimum phase shift) and "flat" frequency responses for both signal and noise. Finally, the detector/amplifier combination was checked to ensure adequate bandwidth for the proposed scan. The strategy of providing maximum gain at the preamplifier ensures that signals remain (as far as possible) shot-noise limited.

The IFS 120 HR FTS utilizes digitally controlled electronic filters and programmable gain amplifiers prior to signal quantization (at 16-bit resolution). It was noted that these components introduce considerable excess noise into the signal and they were accordingly bypassed by utilizing custom analog filters feeding the digitizer directly. The FTS was set to scan at a few selected velocities such that interferograms from all the wave-bands of interest would fall within two temporal frequency bands (3.5 to 7 kHz or 5 to 10 kHz). Eighth order bandpass filters were designed (utilizing MAXIM MAX274 devices) with less than 0.1 dB gain ripple over the pass-band and Bessel-type (constant delay) responses at the band edges to minimize phase distortion. The filters served to limit excess electrical noise from the detection system (including low-frequency " $1/f$ " noise) which would otherwise be "folded in" to the spectra by the aliasing of the FTS (thus raising the apparent noise floor). Because of

TABLE 1
Summary of Experimental Runs and Conditions

	Range (cm ⁻¹)	Scans	<i>p</i> (hPa)	<i>T</i> (K)	<i>l</i> (m)	(2 <i>L</i>) ⁻¹ (cm ⁻¹)	Detector	(S/N) _{max}
1	6500–11000	2560	20.08(8)	294.4(7)	480.8(6)	0.009	InGaAs-diode	
2	9200–12800	2166	22.93(8)	295.7(7)	800.8(10)	0.011	Si-diode	~1750 : 1
3	11800–14500	926	21.15(8)	296.0(7)	800.8(10)	0.013	Si-diode	~1200 : 1
4	13200–16400	3247	23.02(17)	295.4(7)	800.8(10)	0.015	Si-diode	~3500 : 1

the optical prefiltration noted above, these electrical filters were not used to limit the effective optical bandwidth. The steady noise level of the detector and filter combination was below the resolution of the digitizer.

Initial scans were performed for each waveband, and power spectra were computed to establish the noise floor and the maximum optical path difference (*L*) beyond which line-profile accuracy would be actually be degraded rather than improved because the added interferogram points would contain more noise than signal (in addition to wasting time that could have been spent observing usable smaller path differences). The resolving power thus determined was used to select scan lengths and the maximum size of the FTS input aperture.

For unapodized interferograms, the resolution (the distance between statistically independent points) can be shown to be $\delta\tilde{\nu} = \frac{1}{2L}$ (see Thorn *et al.* (19) for a discussion of this point). Resolutions of $\delta\tilde{\nu} = 0.009\text{--}0.015\text{ cm}^{-1}$ were used over optical path lengths of *l* = 480.8 for the near infrared and *l* = 800.8 for the near infrared–visible.

Interferograms were co-added for periods of up to 62 h in order to improve signal-to-noise ratios (limited by lamp aging and disk space). Interferograms were recorded unapodized, and Mertz-type phase correction was applied. The ultimate signal-to-noise ratio in the spectra was about 3500 to 1.

2.2. Experimental Conditions

Gas temperatures in the LPAC were measured using platinum resistance thermometers (PRTs). These have previously been shown to give consistent and representative measurements of the temperature of gases contained within the LPAC inner vessel (18). Baratron pressure gauges, rated at 10 and 1000 Torr, were used during sample preparation and throughout the measurements using the LPAC. The atmospheric pressure reading of the 1000-Torr Baratron was compared with that of a precision aneroid barometer. The low-pressure readings of the 10-Torr gauge were checked by measuring identical pressures with both Baratron gauges. Relative humidity was measured with two humidity gauges positioned at opposite ends of the LPAC. The local vapor temperature at the humidity gauges was recorded using PRTs integrated into the sensors. The measurements were made on pure water vapor at room temperatures. Water vapor samples were prepared from liquid water using a clean glass vacuum line and purified to remove dissolved air using freeze–pump–thaw

cycles. Agreement between the humidity sensor and pressure gauge readings (to within the humidity sensor accuracy of 1%) confirmed the purity of the water vapor under study. After an initial period of approximately 30 min, sample pressures remained stable without change over the period of measurement, indicating that adsorption processes at the cell walls have reached equilibrium.

Besides the total integration time, the three experimental parameters, temperature *T*, sample pressure *p*, and absorption path length *l*, describe the conditions of an individual measurement and their uncertainties determine to a large part the achievable precision of the spectral line parameters. The results for the four main runs are summarized in Table 1.

The temperature inhomogeneity of the LPAC at a given time was smaller than $\pm 0.2\text{ K}$. During an observation, the LPAC temperature drifted by typically less than 0.5 K. A comparison of these readings with the temperature readings provided by the humidity sensors showed the latter to have systematically higher values. The discrepancies were less than 1 K (typically about 0.5 K) and these differences can be explained by an insufficient thermal isolation of the humidity sensors from the outer wall of the cell (the laboratory temperature was usually similar to the temperature readings of the humidity sensors). Given the lower reliability of these readings for the gas temperature, only the PRT readings were used to derive the mean gas temperatures for the observations.

The spatial and temporal mean temperature for given spectrum measurement was calculated as the average of all observations over the time of the measurement. The uncertainty of the mean temperature has two contributions: the uncertainty in the temperature reading and the uncertainty arising from the spatial and temporal temperature variations. The effect of the latter on the mean temperature can be approximated by the standard error of the mean value, which is in all cases smaller than 0.1 K. The temperature uncertainty is mainly determined by the uncertainty in the reading, which can be estimated to be the sum of the quoted accuracies of the sensor and the data logging system. This yields an uncertainty of 0.7 K for the PRT readings of the LPAC.

The pressure measurements for the LPAC observations made using MKS Baratron capacitance gauges were taken at reasonable intervals, typically at the beginning and the end of each day of the measurement. Differences were typically less than 0.1 hPa, which is less than 0.5%. Additionally, the water pressures were

determined from the relative humidity and the tabulated saturation vapor pressure of water at the temperature of the humidity sensor. In each case the weighted mean of all readings were calculated. The errors of the individual readings were estimated to be the sum of the accuracy of the type of sensor as specified by the manufacturer and the temporal change in pressure. A full error analysis using the monitored pressure values yielded typical uncertainties in the water pressure of about 0.5%. The errors of the water pressures derived from the humidity readings were typically 1%.

The path through the multipath cell has two components: a main multireflection path between the cell mirrors and additional paths from the entrance window to the first focus and from the final focus to the exit window. The main mirror separation for the LPAC is $R = 8000(10)$ mm; the small additional component is $d = 746(20)$ mm. The total path l is given by $l = (2n + 2)R + d$, where $(2n + 2)$ is the number of traversals of the light beam inside the cell and n is the number of reflections on the field mirror. This gives path lengths of 480.8(6) m for the lowest frequency run and 800.8(10) m for all other measurements.

3. DATA ANALYSIS

3.1. Baseline Correction

Fourier transformation of each observation yields a single-beam absorption spectrum with lines in absorption against a smooth varying background signal. This background signal was removed, to a first approximation, by taking the ratio of the full to an empty cell signal, if one was measured, to give the corresponding transmittance spectrum, $T(\nu)$. Due to changes in the lamp output during the 12-h observations and other small effects, the empty-cell spectra are not an exact match of the

underlying background signal and systematic departures of the baseline from its true value of 100% transmittance still remain after ratioing. These discrepancies are wavenumber dependent and are typically of the order of up to 1–2%.

An improved baseline was derived by cubic spline interpolation through a set of carefully chosen points along the baseline (15). These points were taken at points on the baseline where there is no obvious absorption by water lines. This is relatively straightforward where the line density is small and the lines are generally well separated. The task is far more difficult for the regions where there are many very strong or saturated lines or the spectrum contains a large number of blended lines. In regions of strong absorption there are large intervals where no clear, unabsorbed windows can be seen; a smoothly varying cubic spline function was used to give the best estimate of the continuum level across these regions. The procedure of baseline correction was performed in several steps to achieve the best possible spectral baseline for the observed transmittance spectrum. The result is typically accurate to better than 10% of the peak-to-peak noise level. The final transmittance spectra were converted to absorbance spectra according to $A(\nu) = -\ln[T(\nu)]$ for input to the spectral line analysis.

Figure 1 makes a comparison of the spectrum analyzed here with other long-pathlength FTS recorded previously at Kitt Peak (5) and Rheims (11). It is clear that, for this spectral region at least, our new spectra are superior. Both the other spectra show effects of nonwhite noise, although this is worse in the Kitt Peak data. The Rheims spectra also show inadequate resolution both in increased linewidths and in ringing at the feet of the two strong lines in the spectral region considered, which obscures some of the weak lines present. It should be noted that as the frequencies move towards the blue ringing is less of a problem in the Rheims data and beyond about $15\,000\text{ cm}^{-1}$ their data appear superior to ours and those from Kitt Peak. However, in the region of present

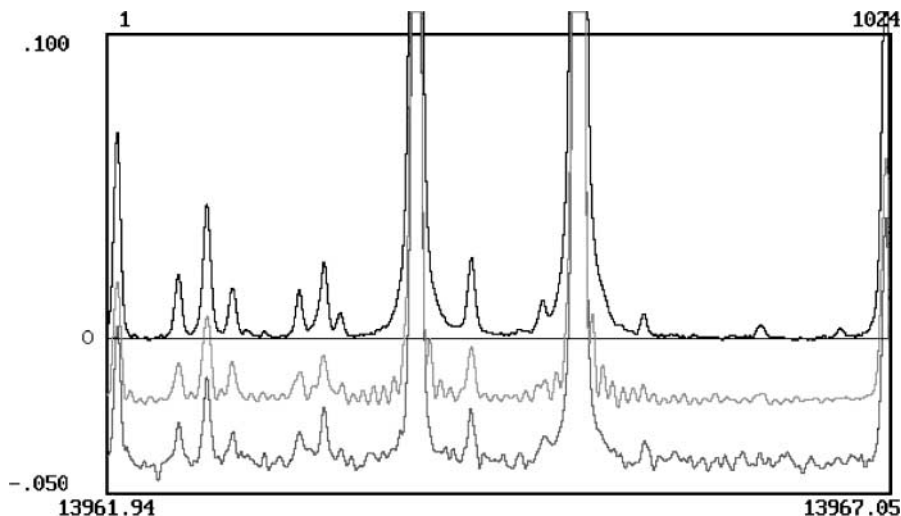


FIG. 1. High-resolution comparison of absorption spectra. The lines from top down are ours (no offset), Rheims (11) (offset -0.02 in absorbance), and Kitt Peak (5) (offset -0.04).

interest, it is clear that our new spectra contain information on many weak lines not obtainable from the previous spectra.

3.2. Line Parameter Retrieval

The line parameters of the individual transitions were determined from the absorbance spectra using an interactive least-squares line-fitting procedure that is part of the GREMLIN spectrum analysis software. The general aim was to fit Voigt line profiles to all lines, such that the residuals of the fit were indistinguishable from the noise. This was usually possible, except when a line was so strong that the peak absorbance approached saturation, and when the wavenumber separation of a pair of lines was so small that the least-squares routine could not find a stable two-line solution. Saturation was a more common problem in the smaller wavenumber regions and simultaneous fitting of up to several tens of lines was necessary.

The molecular lineshape was assumed to be a Voigt line profile, i.e., a convolution of Lorentzian (pressure-broadened) and Gaussian (Doppler-broadened) contributions. Although the Doppler contribution to a Voigt profile caused by the motion of the particles can generally be calculated and only the Lorentzian needs to be fitted, the effect of collisional narrowing (20–22) can be strong enough to seriously distort standard Voigt line profiles; see (23).

Collisional narrowing has been observed for the water molecule for a small number of lines (20–22) and found to vary between 0.005 and 0.015 cm⁻¹ atm⁻¹. Without an exact knowledge of the latter for the majority of lines, the effect can, however, not generally be simulated and included in our line fits. Although there are more complex line profiles based on hard and soft collisional models that include collisional narrowing, it has been shown that “generalized” Voigt profiles, profiles for which both Lorentzian and Gaussian contributions are adjusted, fit observed lineshapes equally well (22). Furthermore, “generalized” Voigt profiles are much faster to compute and less prone to numerical correlations, making them the preferred option for this study. These are factors of particular importance for the fitting of a complex spectrum with thousands of lines and a large number of blends.

In order to achieve the best fit of the lineshapes and to determine precise line intensities, both components were adjusted during the line fits (“generalized” Voigt profile). This procedure has, however, a negative effect on the line broadening information. Whereas the Lorentzian and Gaussian contributions are clearly defined for a “standard” Voigt profile, with the Gaussian contribution given by the temperature and the mass of the absorber molecule and the Lorentzian contribution given by the pressure broadening, the use of the “generalized” Voigt profile degrades the physical meaning of the two contributions. In such a case, a change in the damping parameter (the ratio of the Lorentzian contribution to the total linewidth) may account for second order effects that change the lineshape. Such effects may have technical reasons such as line blending or small baseline

errors, but may also have a physical cause such as an instrumental lineshape contribution or collisional narrowing.

The set of line parameters retrieved for a given line consisted of the line position, ν_{nm} , where m indicates the lower level and n the upper energy level of a transition, the peak absorbance, A_p , the integrated absorbance, A_I , the full line width at half maximum, FWHM, and the damping parameter, D . The uncertainties in the spectral line parameters were estimated using the expressions

$$\frac{\Delta \nu_{nm}}{\text{FWHM}} \sim \frac{\Delta \text{FWHM}}{\text{FWHM}} \sim \frac{\Delta A_I}{A_I} = \frac{k_p}{(S/N)\sqrt{N_W}}, \quad [1]$$

where the signal-to-noise ratio (S/N) is given by the ratio of the peak absorbance to the rms noise at the line position and N_W is the number of statistically independent points in a linewidth, which can be determined from the linewidth and the spectral resolution. The parameter k_p is a constant for a given set of line parameters, where the index p indicates either ν_{nm} , FWHM, or A_I . The above data sets are well represented by $k_{\nu_{nm}} = 0.8$, $k_{\text{FWHM}} = 2.5$, and $k_{A_I} = 2.0$; see the recent book by Davis *et al.* (25) for a discussion of the k constants.

The output from the fitting procedure and the error calculations were then used to derive the line parameters for each individual spectrum.

3.3. Parameters

In this work detailed line parameters are presented for the region 13 200–15 000 cm⁻¹. These were taken from run 4 (see Table 1), which had the highest S/N ratio.

Two points have to be made about the line positions derived from the fits of the water spectra recorded through this study. First, wavenumber calibration was performed using calibration spectra measured at Kitt Peak (5). Second, pressure-induced line shifts usually cause the lines to shift to smaller wavenumber with increasing sample pressure. This effect was not measured and not included. All line positions are pressure-shifted. Self-shifts for water were found (20–22) to vary significantly (in both directions) from line to line and may shift lines by as much as 0.004 cm⁻¹ at a water pressure of 23 hPa.

Integrated line intensities were derived from the integrated absorbances according to

$$S_m^n = \frac{T}{T_0 L_0} \frac{A_I}{p_{\text{H}_2\text{O}} l}, \quad [2]$$

where the Loschmidt number $L_0 = 2.686763(23) \times 10^{19}$ cm⁻³ atm⁻¹ gives the number of particles of an ideal gas at standard pressure $p_0 = 1$ atm and $T_0 = 273.15$ K. The intensities are given in units of cm molecule⁻¹ (HITRAN units). As in HITRAN, no distinction was made between the contributions from the different isotopomers of the water molecule. The error estimates of the line intensities were based on the uncertainties

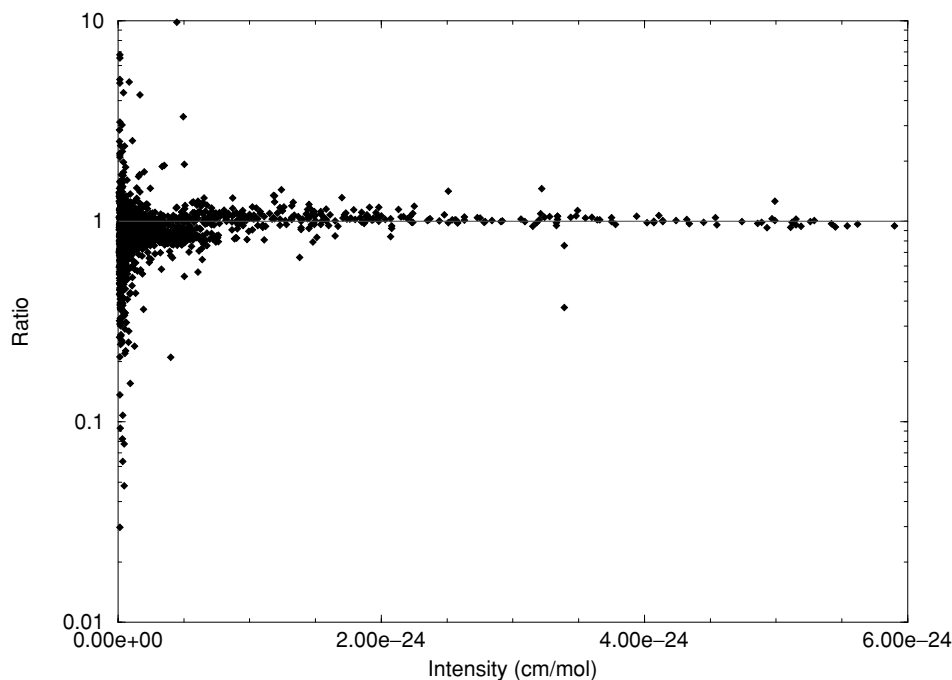


FIG. 2. Comparison of intensities measured in this work with those given the corrected version of HITRAN (I_3) in the frequency range 13 202–15 195 cm^{-1} . Given is the ratio of I (this work) to I (HITRAN) as a function of the intensity measured here.

in the individual parameters and calculated via standard error analysis.

Figure 2 gives a comparison of the line intensities measured here with those present in the corrected version of HITRAN

(I_3). The comparison is made only for lines weaker than $6 \times 10^{-24} \text{ cm molecule}^{-1}$ as lines stronger than this in our spectrum show effects due to approaching saturation. There is good agreement between our data and the corrected HITRAN for

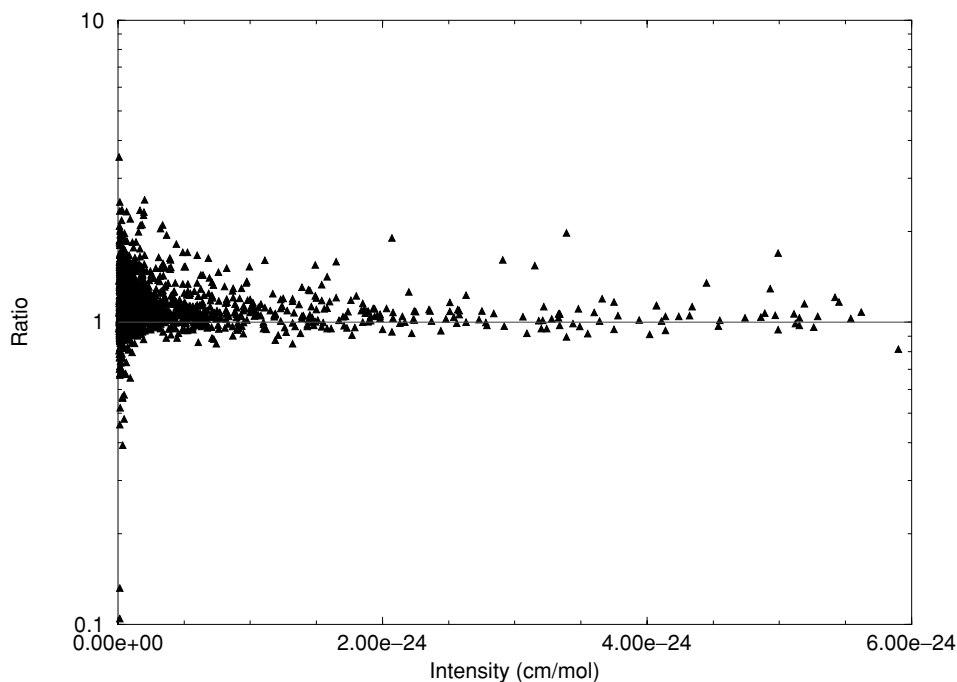


FIG. 3. Comparison of self-broadening coefficients, $\gamma_L(\text{H}_2\text{O})$, measured in this work with those given in HITRAN (I_7) in the frequency range 13 202–15 195 cm^{-1} . Given is the ratio of $\gamma_L(\text{H}_2\text{O})$ (this work) to $\gamma_L(\text{H}_2\text{O})$ (HITRAN) as a function of the line intensity measured here.

lines in the intensity range $1\text{--}6 \times 10^{-24}$ cm molecule $^{-1}$. Lines weaker than this show considerable scatter and some systematic deviation. We believe that our new parameters for these lines should be considerably more accurate than those determined previously.

The derivation of self-induced pressure-broadening coefficients requires the contribution of pressure broadening to the line profile (the Lorentzian contribution) to be evaluated. As mentioned above, the damping parameter (the ratio of the Lorentzian contribution to the total linewidth) derived from a line fit loses its true physical meaning for a “generalized” Voigt profile and the Lorentzian contribution can only be extracted approximately. It follows that we are left without direct information on the Lorentzian contribution to the line profile. The main causes for deviations of the damping parameter from its true value are first that there are very often weak lines blending the line under consideration and second that weak lines at low signal-to-noise ratio are often distorted by the noise. Collisional narrowing is negligible at the water pressures under consideration (about 23 hPa). An empirical estimate was made for its contribution to the linewidth. Simulations show that for a “standard” Voigt profile and pressure-broadening coefficients in the range $\gamma_L(\text{H}_2\text{O}) = 0.1\text{--}0.8$ cm $^{-1}$ atm $^{-1}$ damping parameters $D = 0.11\text{--}0.59$ are expected for the water spectra of this study. Gaussian linewidths are on the order of $0.039\text{--}0.044$ cm $^{-1}$ in the spectral range $13\,350\text{--}15\,000$ cm $^{-1}$. Collisional narrowing of the Doppler width of the order $0.005\text{--}0.015$ cm $^{-1}$ atm $^{-1}$ is only on the order of $0.0001\text{--}0.0004$ cm $^{-1}$. A mean broadening coefficient of $\gamma_L(\text{H}_2\text{O}) = 0.43$ cm $^{-1}$ atm $^{-1}$ can be calculated from the data listed in HITRAN96 (17) and translates to a mean damping parameter of $D = 0.39$. As the broadening parameters are not that critical for weak lines, which are the main aim of this study, a mean damping parameter of $D = 0.39$ seemed the most appropriate and consistent choice for the derivation of broadening parameters. Hence, the Lorentzian contribution to the line profile, FWHM_L , was calculated using $\text{FWHM}_L = D^* \text{FWHM}$, with $D = 0.39$.

The pressure-induced self-broadening coefficient $\gamma_L(\text{H}_2\text{O})$ is given by the Lorentzian contribution to the line profile, FWHM_L , and the total water pressure in the sample cell,

$$\gamma_L(\text{H}_2\text{O}) = \frac{\text{FWHM}_L}{2p(\text{H}_2\text{O})}. \quad [3]$$

The error estimates of the broadening coefficients were based on the uncertainties in the individual parameters and calculated via standard error analysis.

Figure 3 gives a comparison of the self-broadening coefficients measured here with those given in HITRAN (17). Again we only make the comparison for lines weaker than 6×10^{-24} cm molecule $^{-1}$ to avoid problems due to saturation in our spectrum. There is fair agreement between the parameters al-

though ours are on average 13% larger than those in HITRAN. The disagreement is largest for the weakest lines. It is not clear to us which of these HITRAN data correspond to actual experimental determinations and which have been obtained by other means, such as scaling air-broadening coefficients.

4. LINE ASSIGNMENTS

Of the 3604 lines measured in run 4 and analyzed here, 2119 were observed previously by Mandin *et al.* (5), who also measured their absolute intensities, and a further 219 were observed by Carleer *et al.* (11), who did not present absolute intensity information. Where a line had been assigned in the previous studies it was possible to simply copy these assignments.

TABLE 2
Summary of Newly Assigned H_2^{16}O Transitions in the Region
 $13\,200\text{--}15\,000$ cm $^{-1}$

Band		ω [31] (cm $^{-1}$)	Lines	
Local mode	Normal mode		a	This work
(1,0) $^+6$	160			4
(1,0) $^-6$	061	12586.		4
(2,0) $^+4$	240	13205	39	23
(2,0) $^-4$	141	13256.2	71	60
(1,1) 4	042	13453.7	36	33
(3,0) $^+2$	320	13640.7	131	69
(3,0) $^-2$	221	13652.656	300	59
(1,0) $^+7$	170	13661.	5	8
(4,0) $^+0$	400	13828.277	298	67
(4,0) $^-0$	301	13830.938	401	71
(1,0) $^-7$	071	13835.372	6	5
(2,1) $^+2$	122	13910.896	134	49
(2,1) $^-2$	023	14066.194	119	52
(3,1) $^+0$	202	14221.161	274	62
(3,1) $^-0$	103	14318.813	339	47
(2,2) 0	004	14537.504	146	44
(2,0) $^+5$	052			2
(2,0) $^-5$	151	14647.2	21	10
(1,1) $^-5$	250			2
(3,0) $^+3$	330	15108.239	33	22
(3,0) $^-3$	231	15119.028	186	20
(4,0) $^+1$	410	15344.503	174	13
(4,0) $^-1$	311	15347.956	296	26
(2,1) $^+3$	132	15377.7	22	3
(2,1) $^-3$	033	15534.709	113	4
(3,1) $^+1$	212	15742.795	113	16
(3,1) $^-1$	113	15832.765	195	13
(3,0) $^+4$	340	16534.3	48	2
(3,0) $^-4$	241	16546.3	58	5
(4,0) $^-2$	321	16821.635	165	3
(4,0) $^+2$	420	16823.	112	2
(5,0) $^+0$	500	16898.4	182	2
(5,0) $^-0$	401	16898.842	253	4
(2,1) $^-4$	043	16967.5	16	1
(4,1) $^-0$	203	17495.528	209	2
(3,2) $^+0$	104	17748.1	78	1

^a Previously assigned lines from Refs. (5, 11, 26).

However, although considerable effort has been made to make line assignments to the previous experimental studies (5, 11, 26), a significant portion of the previous observations remained unassigned. Thus our newly measured lines were combined with lines measured in previous studies, but still unassigned, to give a dataset of unassigned lines for analysis.

Analysis of this dataset was accomplished in a number of steps. First obvious, “trivial” assignments were made; we define trivial assignments as ones to upper levels whose energies have already been determined experimentally. Further assignments were then made by comparison with variational linelists for which those due to Partridge and Schwenke (24) was used. These comparisons enabled us to assign many transitions due to H_2^{16}O plus 42 due to H_2^{18}O and 6 due to H_2^{17}O . The H_2^{17}O assignments are the first time such transitions have been seen in a long-path-length water spectrum recorded at natural abundance. As H_2^{17}O is present at less than 0.04% H_2^{16}O , these observations underline the sensitivity of the techniques used here. Spectra of isotopically enriched water exist in the Kitt Peak archive (see (29)) and these have been used to confirm that our isotopomer identifications are indeed correct. These archived spectra provide a much better starting point for analysis of H_2^{18}O and H_2^{17}O spectra; work on this is currently under way (30).

Even after this process was complete, there were still a large number of unassigned transitions in our dataset. A more systematic, computationally driven procedure was therefore followed

for H_2^{16}O . First all possible trivial assignments, including those arising from possible hot bands, were identified. The remaining unassigned lines were then analyzed electronically for transitions linked by combination differences. This procedure threw up a large number of candidate assignments which were then assessed by comparing the tentative upper state energy level with levels of the same symmetry in Partridge and Schwenke’s (24) list of energy levels. This procedure produced many assignments but care had to be taken with the vibrational quantum numbers which are not reliably given in the energy level compilation. In particular we found a number of candidate transitions to the (080) state of H_2^{16}O but uncertainty over the energy levels of this state prevented us confirming these tentative assignments. Our analysis threw up three cases where transitions, those at 13 835.69, 15 213.49, and 15 489.34 cm^{-1} , had been misassigned in previous studies. In each case the previous assignment had not been confirmed by combination differences and was replaced by a new assignment which could be confirmed in this fashion.

Table 2 summarizes our 952 new assignments to H_2^{16}O transitions. We note that the transitions are spread across 35 different upper vibrational states. A full list of measured lines is given in the journal’s electronic archive. A total of 676 lines remain unassigned. A file of 191 lines newly assigned to the previous (5, 11) spectra is also given in the archive. New line assignment of course can also lead to new, experimentally determined energy levels. The H_2^{16}O assignments presented here have been included

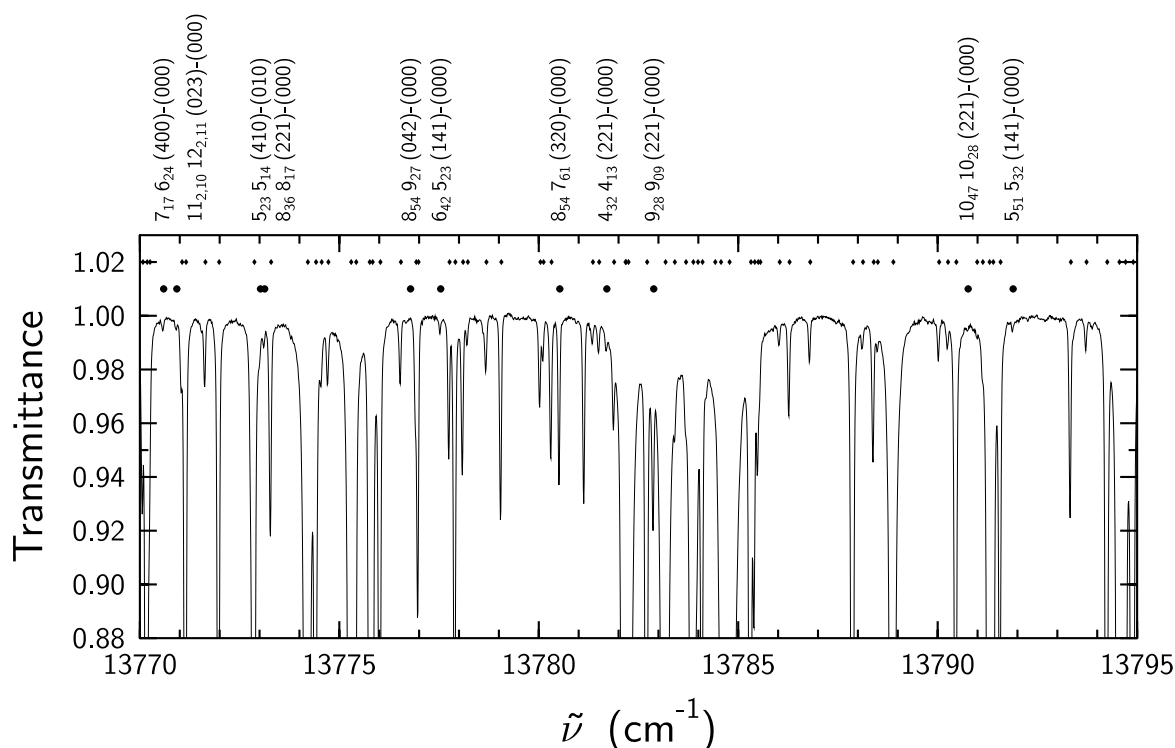


FIG. 4. Sample spectrum plus new line assignments. The small diamonds at the top of the spectrum denote previously assigned lines; newly assigned lines have assignments above the figure and are marked by filled circles for H_2^{16}O lines.

10. J.-M. Flaud, C. Camy-Peyret, A. Bykov, O. Naumenko, T. Petrova, A. Scherbakov, and L. Sinitsa, *J. Mol. Spectrosc.* **185**, 211–221 (1997).
11. M. Carleer, A. Jenouvrier, A.-C. Vandaele, P. F. Bernath, M. F. Mérienne, R. Colin, N. F. Zobov, O. L. Polyansky, J. Tennyson, and A. V. Savin, *J. Chem. Phys.* **111**, 2444–2450 (1999).
12. N. F. Zobov, D. Belmiloud, O. L. Polyansky, J. Tennyson, S. V. Shirin, M. Carleer, A. Jenouvrier, A.-C. Vandaele, P. F. Bernath, M. F. Mérienne, and R. Colin, *J. Chem. Phys.* **113**, 1546–1552 (2000).
13. L. P. Giver, C. Chackerian Jr., and P. Varanasi, *J. Quant. Spectrosc. Radiat. Transfer* **66**, 101–105 (2000).
14. D. Belmiloud, R. Schermaul, K. Smith, N. F. Zobov, J. Brault, R. C. M. Learner, D. A. Newnham, and J. Tennyson, *Geophys. Res. Lett.* **27**, 3703–3706 (2000).
15. R. Schermaul, R. C. M. Learner, D. A. Newnham, R. G. Williams, J. Ballard, N. F. Zobov, D. Belmiloud, and J. Tennyson, *J. Mol. Spectrosc.* **208**, 32–42 (2001).
16. R. Schermaul, R. C. M. Learner, D. A. Newnham, J. Ballard, N. F. Zobov, D. Belmiloud, and J. Tennyson, *J. Mol. Spectrosc.* **208**, 43–50 (2001).
17. L. S. Rothman, C. P. Rinsland, A. Goldman, S. T. Massie, D. P. Edwards, J.-M. Flaud, A. Perrin, C. Camy-Peyret, V. Dana, J.-Y. Mandin, J. Schroeder, A. McCann, R. R. Gamache, R. B. Wattson, K. Yoshino, K. V. Chance, K. W. Jucks, L. R. Brown, V. Nemtchinov, and P. Varanasi, *J. Quant. Spectrosc. Radiat. Transfer* **60**, 665–710 (1998).
18. J. Ballard, K. Strong, J. J. Remedios, M. Page, and W. B. Johnston, *J. Quant. Spectrosc. Radiat. Transfer* **52**, 677–691 (1994).
19. A. Thorn, U. Litzen, and S. Johansson, “Spectrophysics,” p. 196, Springer-Verlag, Berlin, New York, 1999.
20. B. E. Grossmann and E. V. Browell, *J. Mol. Spectrosc.* **136**, 264–294 (1989).
21. B. E. Grossmann and E. V. Browell, *J. Mol. Spectrosc.* **138**, 562–595 (1989).
22. P. L. Ponsardin and E. V. Browell, *J. Mol. Spectrosc.* **185**, 58–70 (1997).
23. R. Schermaul and R. C. M. Learner, *J. Quant. Spectrosc. Radiat. Transfer* **61**, 781–794 (1999).
24. H. Partridge and D. W. Schwenke, *J. Chem. Phys.* **106**, 4618–4639 (1997).
25. S. P. Davis, M. C. Abrams, and J. W. Brault, “Fourier Transform Spectrometry,” Academic Press, San Diego, 2001.
26. O. L. Polyansky, N. F. Zobov, S. Viti, and J. Tennyson, *J. Mol. Spectrosc.* **189**, 291–300 (1998).
27. O. L. Polyansky, N. F. Zobov, S. Viti, J. Tennyson, P. F. Bernath, and L. Wallace, *Science* **277**, 346–349 (1997).
28. O. L. Polyansky, N. F. Zobov, J. Tennyson, J. A. Lotoski, and P. F. Bernath, *J. Mol. Spectrosc.* **184**, 35–50 (1997).
29. J.-P. Chevillar, J.-Y. Mandin, J.-M. Flaud, and C. Camy-Peyret, *Can. J. Phys.* **65**, 777–789 (1987).
30. M. Tanaka, J. W. Brault, and J. Tennyson, to be submitted.
31. J. Tennyson, N. F. Zobov, R. Williamson, O. L. Polyansky, and P. F. Bernath, *J. Phys. Chem. Ref. Data* **30**, 735–831 (2001).
32. W. Zhong, J. D. Haigh, D. Belmiloud, R. Schermaul, and J. Tennyson, *Q. J. R. Meteorol.* **127**, 1615–1626 (2001).